# Coherent Phonon Dynamics in Semiconducting Carbon Nanotubes: A Quantitative Study of Electron-Phonon Coupling

Larry Lüer,[1] Christoph Gadermaier,[2] Jared Crochet,[3] Tobias Hertel,[3] Daniele Brida,[1] and Guglielmo Lanzani[4]

[1]*National Laboratory for Ultrafast and Ultraintense Optical Science, INFM-CNR, Dipartimento di Fisica, Politecnico di Milano, Piazza L. da Vinci 32, 20133 Milano, Italy*

[2]*Department of Complex Matter, Jozef-Stefan Institute, Jamova 39, 1000 Ljubljana, Slovenia*

[3]*Institut für Physikalische Chemie, Universität Würzburg, Am Hubland, 97074 Würzburg, Germany*

[4]*Italian Institute of Technology and Dipartimento di Fisica, Politecnico di Milano, Piazza L. da Vinci 32, 20133 Milano, Italy*

(Received 14 August 2008; published 24 March 2009)

We excite and detect coherent phonons in semiconducting (6, 5) carbon nanotubes via a sub-10-fs pump-probe technique. Simulation of the amplitude and phase profile via time-dependent wave packet theory yields excellent agreement with experimental results under the assumption of molecular excitonic states and allows determining the electron-phonon coupling strength for the two dominant vibrational modes.

DOI: 10.1103/PhysRevLett.102.127401 PACS numbers: 78.47.J−, 73.22.−f, 78.47.Fg

Electron-phonon (*e*-ph) coupling is at the heart of many phenomena in condensed matter physics, such as carrier scattering in transport, superconductivity, excited state relaxation, and Raman scattering. Despite its ubiquity, its experimental quantification is not straightforward. While in most crystalline solids *e*-ph coupling is a small perturbation, leading to a tiny nuclear displacement upon electronic excitation, in molecules it is a dominating interaction. For instance, strong vibrational replicas are seen in optical spectra. One-dimensional systems, such as single wall carbon nanotubes [1] (SWCNTs) are in between these two extremes, because of the excitonic nature of the excited states [2–4]. One should thus expect strong evidence of *e*-ph dynamics. However, most SWCNT samples contain a broad distribution of tube types of different chirality vectors $(n, m)$, which correspond to different optical resonances [1,5]; this hampers a detailed understanding of their fundamental properties. By using a particular preparation known as the cobalt-molybdenum catalytic (COMOCAT) method [6], less polydisperse samples can be obtained, with predominance of the (6, 5) semiconducting tube. With further processing of separation and extraction, highly enriched samples can be obtained [7,8]. This allows the investigation of fundamental mechanisms previously obscured by spectral congestion, without the experimental complication of single molecule spectroscopy.

A value for *e*-ph coupling to longitudinal acoustic modes has been determined for metallic carbon nanotubes (CNTs) by femtosecond electron relaxation [9] as well as for the *G* mode from the broadening of Raman lines [10]. For semiconducting CNTs, the *e*-ph coupling of the radial breathing mode (RBM) has been quantified from comparing the excitation profile of the first and second harmonics of the Raman excitation profile [11]. This method works with reasonable accuracy only for the nanotube family with chiral $\nu = \mathrm{mod}(n - m, 3) = -1$. Values for the RBM for $\nu = +1$ and for the *G* mode are elusive.

We study *e*-ph coupling in the time domain by coherent phonon spectroscopy [12–14]. Two modes can be impulsively excited, both assigned to the semiconducting tube: the RBM and the *G* mode, both assigned and well known from standard Raman spectroscopy [15–17]. We detect amplitude and phase profiles for the coherent oscillations upon the probing wavelength. In the framework of a molecular approach, based on the conjecture that one-dimensional excitons behave like molecular states [18–20], we show that the broad coherent phonon profiles indeed originate only from (6, 5) tubes and contain a *G*-mode replica on the long wavelength side. From this modeling we individually determine the dimensionless *e*-ph coupling constant $\Delta$ for both the RBM and *G* mode of semiconducting SWCNTs on the example of the (6, 5) tube from the $\nu = +1$ family.

We use sub-10-fs broadband visible pulses that are resonant with the second exciton transition in the (6, 5) tube. Details about our setup and the working principle of our technique can be found in Ref. [21].

The study is carried out using colloidal COMOCAT/Na-cholate suspensions obtained by density gradient ultracentrifugation followed by extraction of the original compound in the supernatant. Semiconducting (6, 5) CNTs from this process are dispersed in a xerogel where they display negligible intertube interaction. The sample composition in absorbance spectral weights is (6, 5), 70%; (8, 3), 10%; (6, 4), 10%; (7, 5), 2%; (8, 4), 2% (in percentage of semiconducting tubes).

A characteristic linear absorption spectrum for the studied samples is shown in Fig. 1. The high chiral selectivity is evident from the prominent absorption peaks at 996 and 570 nm, which correspond to the first and second exciton resonance, respectively, for the (6, 5) semiconducting tube.

Pump-probe spectra are shown in Fig. 2(a). The pump pulse populates the second exciton state, causing bleaching

 

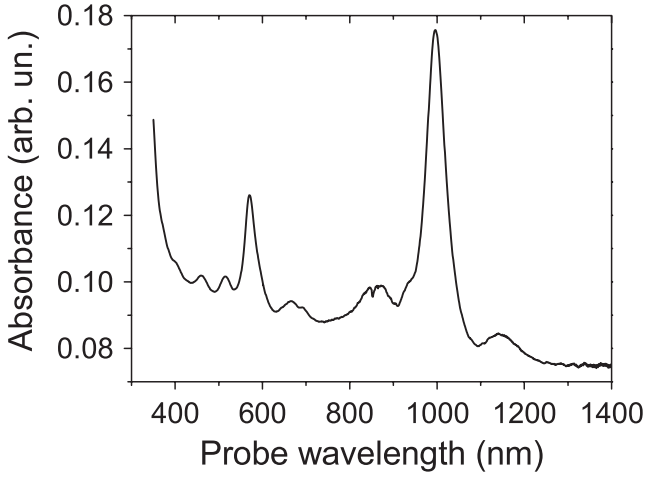


FIG. 1. Absorption spectrum of the COMOCAT SWCNT sample in xerogel.

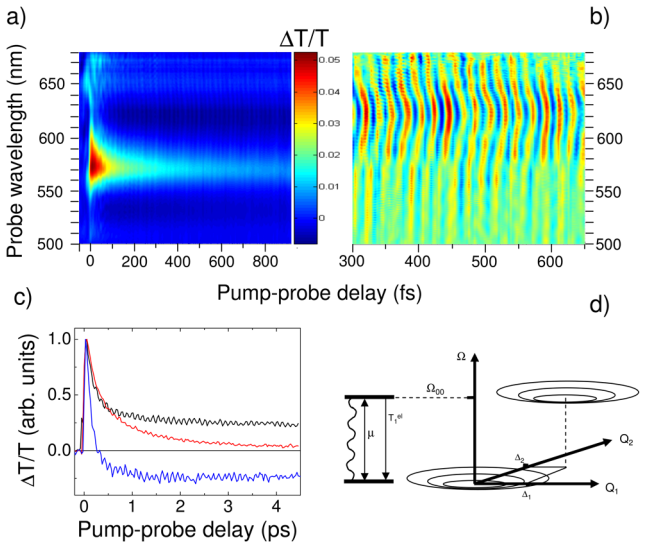


FIG. 2 (color online). (a) 2D map of $\Delta T/T(\tau, \lambda_{pr})$; (b) 2D map of the oscillatory component of $\Delta T/T(\tau, \lambda_{pr})$; (c) differential transmission dynamics at selected wavelengths (black 560 nm, red 580 nm, blue 600 nm); (d) scheme of impulsive wave packet excitation in a two-level system, where the electronic energy $\Omega$ of a PES is given as a function of two normal coordinates $Q_1$ and $Q_2$. The PES of the excited state (electronic excitation energy $\Omega_{00}$) is displaced by $\Delta_1$ and $\Delta_2$ The states are coupled by an optical transition dipole moment $\mu$ leading to a electronic relaxation time $T_1^{el}$.

of the optical transition [22,23]. The initial relaxation of this bleach is extremely fast, with a time constant of about 40 fs [24], followed by a slower bleach recovery in the range of a few hundred femtoseconds. The fast decay is caused by intersubband recombination to the first excitonic state, whose decay to the ground state can be traced by the slower bleach recovery.

After subtraction of the population contribution from the pump-probe spectra, we obtain 2D maps as in Fig. 2(b), showing a clear oscillation pattern. This pattern is the signature of coherent vibrations generated by the impulsive excitation with the sub-10-fs pump pulse. Time traces at selected wavelengths are displayed in Fig. 2(c). One sees that the oscillations are long lived, with damping times associated to the dephasing of vibrational coherence, roughly in the picosecond time scale. Further analysis should be done in the frequency domain. Figure 3(a) shows the Fourier transform of the oscillations in a 2D plot versus probing wavelength. This plot identifies two modes: the RBM [25] at 307 $cm^{-1}$ and the $G$ mode at 1596 $cm^{-1}$. Additional weak modes at 1100 and 2100 $cm^{-1}$ are displayed as well, whose frequency difference to the $G$ mode (500 $cm^{-1}$) is, however, not related to the RBM mode; in the modeling, these modes will therefore be disregarded. In contrast to previous studies, the dependence on the probing wavelength is now well displayed for both the RBM and the $G$ mode. Both modes show a main dip at about 570 nm, which corresponds to the wavelength of the second excitonic transition for the (6, 5) tube, and further minima and maxima at both longer and shorter wavelengths. In order to verify the origin of these features, we zoom into the RBM range of Fig. 3(a), which is a clear fingerprint of the nanotube chirality [Fig. 3(c)]. We find strong RBM amplitude for probe wavelengths ranging from 520 to 660 nm. With respect to the frequency axis, all features show a peak close to 307 $cm^{-1}$, showing that RBM activity over the whole wavelength range should be attributed to the (6, 5) tube, via phonon replicas and/or inhomogeneous broadening.

One may note the similarity between these coherent phonon Fourier spectra and the more usual Raman excitation profiles. Before continuing this discussion, it is important to bear in mind the differences between them [21]. $e$-ph coupling modulates the electronic resonance energy during the vibration. In other words, the impulsive excitation (pulse duration $\ll$ vibrational period) generates a nuclear wave packet propagating on the potential energy surface according to a ''sinusoidal'' quasiclassical trajectory [21,26]. In the pump-probe time traces at fixed probe energy, this translates into an amplitude modulation which is strongest where the slope of the electronic resonance is strongest. Therefore, the probe wavelength dependence of coherent oscillations follows the *first derivative* of the electronic resonance. Peaks in the Raman profile then correspond to minima in the coherent oscillation profile. Figures 4(a) and 4(c) show the experimental amplitude profile for the RBM and the $G$-mode coherent phonon, respectively, and the associated phase. Amplitudes are obtained as cuts through the 2D plot of the Fourier spectra. For the RBM data, there is a clear zero at the second exciton (EX2) resonance and two lobes that develop at longer and shorter wavelength, rather symmetrically. At the resonance dip, a $\pi$ phase flip is detected. For the $G$ phonon, the profile is broader and more structured, with

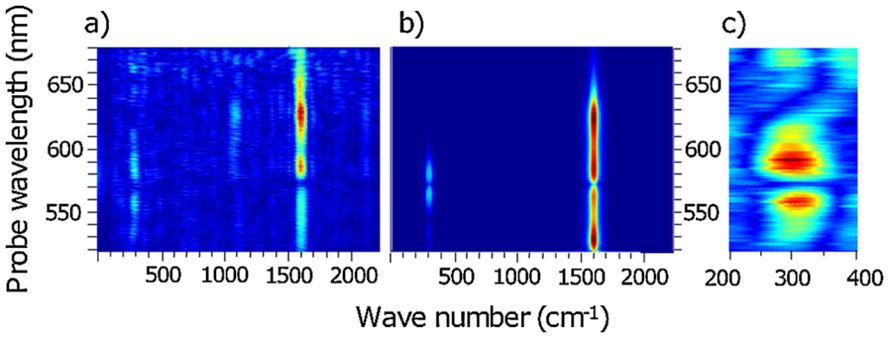


FIG. 3 (color online). (a) Experimental and (b) calculated Fourier spectrum of the coherent oscillations in Fig. 2(b) as a function of probe wavelength. (c) A zoom into the RBM region of (a).

again a clear dip at the EX2 resonance, followed by a secondary structure at longer wavelength. Here too we detect a clear $\pi$ phase jump that marks the underlying zero-phonon electronic resonance.

Better insight can be gained from quantum mechanical simulations, which reproduce both the excitation and the probing process. A simple algorithm for this has been developed a few years ago, based on the time-dependent wave packet theory for the molecular vibronic response [27,28]. We work out simulations in the two-electronic-level approximation, with two coupled vibrations, as sketched in Fig. 2(d). We consider potential energy surfaces (PESs) as a function of the two prominent normal coordinates $Q_{\mathrm{RBM}}$ and $Q_G$. Within the linear $e$-ph coupling approximation, the vibrational frequencies and thus the curvature of both PESs are identical. Only the equilibrium position is changing upon going from the ground to the excited state, by a displacement that is usually expressed in dimensionless units as $\Delta_{\mathrm{RBM}}$ and $\Delta_G$ for the RBM and $G$ mode, respectively [13]. The pulse spectrum used in the simulation is the true one obtained by direct measurement during experiments. The coherence generation mechanism that we consider is the impulsive stimulated resonant Raman scattering. The dephasing time $T_2$, giving rise to the damping of the coherent oscillation in time, is another adjustable parameter of the simulation which is correlated to the Raman linewidth. In Fig. 3(b), we report the calculated 2D plot, which shows good qualitative agreement with the experimental map, reproducing all prominent features, by using a dephasing time of $(2.5 \pm 0.5)$ ps for the RBM and $(400 \pm 100)$ fs for the $G$ phonon, and dimensionless displacement $\Delta_{\mathrm{RBM}} = 0.15$ and $\Delta_G = 0.9$ (see below for how we refine the experimental determination of $e$-ph coupling). Recent results on the $G$-mode phonon lifetime ($T_1$), as measured by anti-Stokes Raman scattering [29], indicate $T_1 = 1$ ps. We find that $T_2$ is shorter than $T_1$, probably due to a number of scattering events that change the phase of the phonon without affecting its population.

Figures 4(b) and 4(d) show that both phase and amplitude are reproduced. Deviations in the $G$ mode may be caused by the slightly chirped probe pulse and by the noise level rising up at the border regions. Nevertheless, the simulated phase correctly reproduces the $\pi$ jump which marks the phononless electronic resonance for both modes. Note that there is a small offset of ca. 2.5 nm between the experimental phase flips of the RBM and $G$ modes, which is, however, not systematic but marks the wavelength resolution of the experiment.

The $G$-mode amplitude profile is distributed on a large spectral range, from 520 to 640 nm. Such a spectral broadening is well reproduced by our quantum mechanical simulation, showing that inhomogeneous broadening and energy transfer are not required for its interpretation. The simulation offers a handle for estimating the $e$-ph coupling strength of the EX2 transition with the two modes. In Fig. 5, we plot simulated spectra of the long wavelength side of the $G$-mode amplitude profile. After normalization at the first structure, one sees that the amplitude of the second peak depends clearly on the $e$-ph coupling strength (here again expressed as displacement). Furthermore, also the minimum of the modulation depth at the wavelength of the phase flip depends strongly on the coupling parameter.

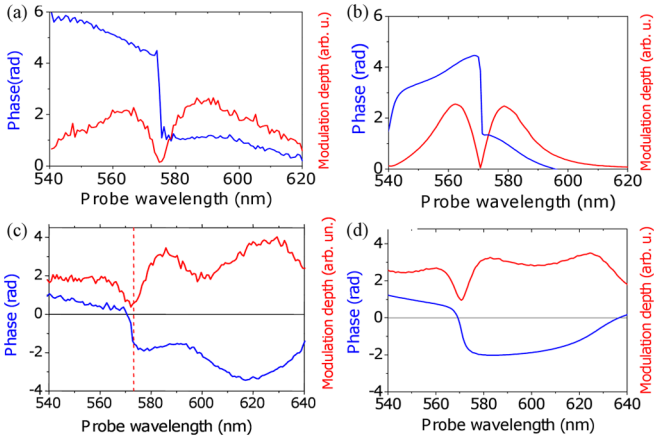


FIG. 4 (color online). Experimental amplitude (red) and phase (blue) profiles of the (a) RBM and (c) $G$-mode coherent oscillations. The corresponding simulated profiles are (b) for the RBM and (d) for the $G$ mode.

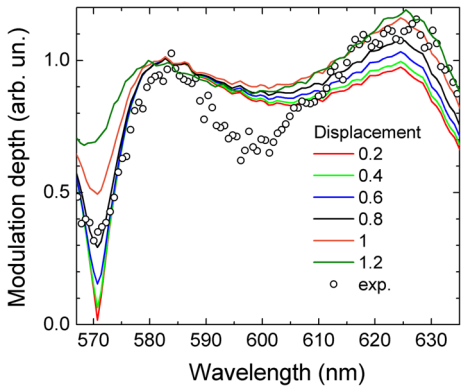


FIG. 5 (color online). Calculated amplitude profile of the $G$ mode for different $e$-ph coupling parameters. The curves are normalized to their primary maximum. Circles: Experimental data.

Comparing simulation and experiment, we estimate a value $\Delta_G = 0.9 \pm 0.2$. Keeping this value fixed, we look at the relative intensity of the RBM modulation depth and obtain a value $\Delta_{\mathrm{RBM}} = 0.15$–$0.3$.

In conclusion, by using sub-10-fs optical pulses we generate coherent phonons in $(6, 5)$ semiconducting SWCNT by impulsive stimulated Raman scattering. We detect transient oscillations in transmission and report the spectral dependence of their amplitude and phase. Quantum mechanical simulations within the molecular approach are in good correspondence with experiments and allow estimating the $e$-ph coupling strength. The value for RBM coupling is within that predicted by theory, while that for the $G$ mode is slightly larger (0.9 instead of 0.4). From the dimensionless displacements, we obtain Huang-Rhys factors $S_{\mathrm{RBM}} = 0.028 \pm 0.017$ and $S_G = 0.4 \pm 0.2$, which place the RBM in the small and the $G$ mode in the medium coupling regime.

C. G. acknowledges Grant No. EIF-040958A from the European Commission. The financial support of the European Commission (Marie-Curie RTN BIMORE, Grant No. MRTN-CT-2006-035859) and the Italian ministry of education (FIRB-SYNERGY No. RBNE03S7XZ) is also acknowledged.

[1] R. Saito, G. Dresselhaus, and M. S. Dresselhaus, *Physical Properties of Carbon Nanotubes* (Imperial College Press, London, 1998).
[2] L. Lüer, S. Hoseinhkani, D. Polli, J. Crochet, T. Hertel, and G. Lanzani, Nature Phys. **5**, 54 (2009).
[3] C. D. Spataru, S. Ismail-Beigi, L. X. Benedict, and S. G. Louie, Phys. Rev. Lett. **92**, 077402 (2004).
[4] E. Chang, G. Bussi, A. Ruini, and E. Molinari, Phys. Rev. Lett. **92**, 196401 (2004).
[5] R. B. Weisman and S. M. Bachilo, Nano Lett. **3**, 1235 (2003).
[6] S. M. Bachilo, L. Balzano, J. E. Herrera, F. Pompeo, D. E. Resasco, and R. B. Weisman, J. Am. Chem. Soc. **125**, 11 186 (2003).
[7] M. S. Arnold, S. I. Stupp, and M. C. Hersam, Nano Lett. **5**, 713 (2005).
[8] Z. Zhu, J. Crochet, M. S. Arnold, M. C. Hersam, H. Ulbricht, D. Resasco, and T. Hertel, J. Phys. Chem. C **111**, 3831 (2007).
[9] T. Hertel and G. Moos, Phys. Rev. Lett. **84**, 5002 (2000).
[10] M. Lazzeri, S. Piscanec, F. Mauri, A. C. Ferrari, and J. Robertson, Phys. Rev. B **73**, 155426 (2006).
[11] Y. Yin, A. N. Vamivakas, A. G. Walsh, S. B. Cronin, M. S. Ünlü, B. B. Goldberg, and A. K. Swan, Phys. Rev. Lett. **98**, 037404 (2007).
[12] L. Dhar, J. A. Rogers, and K. A. Nelson, Chem. Rev. **94**, 157 (1994).
[13] A. Gambetta, C. Manzoni, E. Menna, M. Meneghetti, G. Cerullo, G. Lanzani, S. Tretiak, A. Piryatinsky, A. Saxena, R. L. Martin, and A. R. Bishop, Nature Phys. **2**, 515 (2006).
[14] Y. S. Lim, K. J. Yee, J. H. Kim, E. H. Haroz, J. Shaver, J. Kono, S. K. Doorn, R. G. Hauge, and R. E. Smalley, Nano Lett. **6**, 2696 (2006).
[15] A. M. Rao *et al.*, Science **275**, 187 (1997).
[16] H. Kataura, Y. Kumazawa, Y. Maniwa, I. Umezu, S. Suzuki, Y. Ohtsuka, and Y. Achiba, Synth. Met. **103**, 2555 (1999).
[17] A. Jorio, R. Saito, J. H. Hafner, C. M. Lieber, M. Hunter, T. McClure, G. Dresselhaus, and M. S. Dresselhaus, Phys. Rev. Lett. **86**, 1118 (2001).
[18] T. Ando, J. Phys. Soc. Jpn. **66**, 1066 (1997).
[19] F. Wang, G. Dukovic, L. E. Brus, and T. F. Heinz, Science **308**, 838 (2005).
[20] J. Maultzsch, R. Pomraenke, S. Reich, E. Chang, D. Prezzi, A. Ruini, E. Molinari, M. S. Strano, C. Thomsen, and C. Lienau, Phys. Status Solidi B **243**, 3204 (2006).
[21] *Coherent Vibrational Dynamics*, edited by S. De Silvestri, G. Cerullo, and G. Lanzani (CRC, Boca Raton, 2007).
[22] J.-S. Lauret, C. Voisin, G. Cassabois, C. Delalande, Ph. Roussignol, O. Jost, and L. Capes, Phys. Rev. Lett. **90**, 057404 (2003).
[23] O. J. Korovyanko, C.-X. Sheng, Z. V. Vardeny, A. B. Dalton, and R. H. Baughman, Phys. Rev. Lett. **92**, 017403 (2004).
[24] C. Manzoni, A. Gambetta, E. Menna, M. Meneghetti, G. Lanzani, and G. Cerullo, Phys. Rev. Lett. **94**, 207401 (2005).
[25] Y.-S. Lim, K.-J. Yee, J.-H. Kim, E. H. Hároz, J. Shaver, J. Kono, S. K. Doorn, R. H. Hauge, and R. E. Smalley, Nano Lett. **6** 2696 (2006).
[26] H. L. Fragnito *et al.*, Chem. Phys. Lett. **160**, 101 (1989).
[27] A. T. N. Kumar, F. Rosca, and P. M. Champion, J. Chem. Phys. **114**, 701 (2001).
[28] A. T. N. Kumar, F. Rosca, A. Widom, and P. M. Champion, J. Chem. Phys. **114**, 6795 (2001).
[29] D. Song, F. Wang, G. Dukovic, M. Zheng, E. D. Semke, L. E. Brus, and T. F. Heinz, Phys. Rev. Lett. **100**, 225503 (2008).